Research Article

A three-dimensional colocalization RNA interference screening platform to elucidate the alternative lengthening of telomeres pathway

Sarah Osterwald[1], Stefan Wörz[2], Jürgen Reymann[3], Frank Sieckmann[4], Karl Rohr[2], Holger Erfle[3] and Karsten Rippe[1]

[1] Research Group Genome Organization and Function, DKFZ and BioQuant, Heidelberg, Germany
[2] Department of Bioinformatics and Functional Genomics, Biomedical Computer Vision Group, DKFZ, University of Heidelberg, BioQuant and IPMB, Heidelberg, Germany
[3] ViroQuant-CellNetworks RNAi Screening Facility, University of Heidelberg and BioQuant, Heidelberg, Germany
[4] Leica Microsystems CMS GmbH, Mannheim, Germany

A high-content colocalization RNA interference screen based on automatic three-color confocal fluorescence microscopy was developed to analyze the alternative lengthening of telomeres (ALT) pathway. Via this pathway telomerase-negative cancer cells can maintain their telomeres and with it their unlimited proliferative potential. A hallmark of ALT cells is the colocalization of promyelocytic leukemia (PML) nuclear bodies with telomeres to form ALT-associated PML nuclear bodies (APBs). In our screen, the presence of APBs was used as a marker to identify proteins required for the ALT mechanism. A cell-based assay and an automatic confocal image acquisition procedure were established. Using automatic image analysis based on 3D parametric intensity models to identify APBs, we conducted an unbiased and quantitative analysis of nine different candidate genes. A comparison with the literature and manual analysis of the gene knockdown demonstrates the reliability of our approach. It extends the available repertoire of high-content screening to studies of cellular colocalizations and allows the identification of candidate genes for the ALT mechanism that represent possible targets for cancer therapy.

Received 17 December 2010
Revised 3 March 2011
Accepted 4 April 2011

Supporting information available online

Keywords: 3D colocalization · ALT · Automatic image analysis · RNAi screen · Telomeres

1 Introduction

Microscopy-based high-content screening (HCS) is the automated analysis of spatial and temporal changes in cells using mostly fluorescence signals as readout [1]. RNA interference (RNAi) has become the method of choice to systematically knockdown genes in mammalian tissue culture cells for HCS [2]. Using solid-phase reverse transfection on cell microarrays, hundreds or even thousands of small interfering RNAs (siRNAs) complexed with a transfection reagent can be printed at defined locations on glass slides [3, 4]. Cells are plated on the dried slides to yield cell clusters with a specific gene perturbation in a lawn of non-transfected cells. Depending on the desired readout, proteins and cellular structures are labeled using fluorescent proteins, immunofluorescence procedures or membrane- and DNA-specific synthetic fluorophores. The response of the cells, living or fixed, to the treatment is then imaged to identify phenotypic changes [5]. To this end, large amounts of widefield microscopy images are stored and processed

Correspondence: Dr. Karsten Rippe. Research Group Genome Organization and Function, DKFZ and BioQuant, Im Neuenheimer Feld 280, 69120 Heidelberg, Germany
E-mail: Karsten.Rippe@dkfz.de

Abbreviations: ALT, alternative lengthening of telomeres; **APB**, ALT-associated PML nuclear body; **DAPI**, 4',6-diamidino-2'-phenylindole; **FACS**, fluorescence activated cell sorting; **GFP**, green fluorescent protein; **HCS**, high-content screening; **KS**, Kolmogorov-Smirnov; **PML**, promyelocytic leukemia; **PML-NB**, PML nuclear body; **RNAi**, RNA interference; **ROI**, region-of-interest; **siRNA**, small interfering RNA; **SUMO**, small ubiquitin-like modifier; **TRF1/2**, telomere repeat binding factor 1/2

in order to extract the desired information. Typically, the analysis workflow involves segmentation-based cell identification, feature-based phenotype classification and a quantification of the effect of a certain siRNA by computing the phenotype penetrance under the respective treatment [6]. This approach has already provided valuable systemic data of biological processes such as the cell cycle or virus infection that are relevant in basic research as well as for drug discovery [7, 8]. Technical advancements with respect to image acquisition offer great potential for the spatially resolved characterization of nuclear subcompartments on the submicrometer scale.

Here, we report on the development of a fully automated high-resolution confocal screening platform for 3D colocalization studies to elucidate the mechanism responsible for alternative lengthening of telomeres (ALT). Telomere length maintenance is essential for the unlimited proliferation of cells due to the 3′-end erosion intrinsic to replication of linear chromosomes. Progressive telomere shortening in somatic cells can lead to the induction of senescence or apoptosis, thus acting as a barrier to unlimited proliferation and tumorigenesis. Accordingly, inhibition of telomere length maintenance is considered an important goal in tumor therapy. Most cancer cells reactivate the reverse transcriptase telomerase to maintain their telomeres [9]. However, 10–15% of cancer cells, in particular sarcomas of mesenchymal origin, use instead the recombination-based ALT pathway [10, 11]. Furthermore, treatment of telomerase-positive tumors with telomerase inhibitors could select for those cells within the cancer cell population that are capable to survive via the ALT mechanism [12].

The ALT pathway is characterized by (i) a highly heterogeneous telomere length, (ii) the presence of extrachromosomal telomeric repeats, and (iii) the occurrence of ALT-associated promyelocytic leukemia (PML) nuclear bodies (APBs). APBs are nuclear subcompartments of 0.1–1 μm in size, in which the PML protein assembles in a cap-like structure around the telomeres [13]. Telomere shortening after knockdown of genes involved in the ALT pathway is accompanied by a reduction of APBs [14, 15]. Therefore, APBs were used as a marker for ALT activity to identify genes involved in the ALT mechanism by RNAi [16]. Previous manual widefield image acquisition and evaluation only allowed studying the general effect of a limited number of genes on the formation of the relatively large APBs detected in these experiments. To systematically identify proteins that are required for the formation of APBs in a more reliable and quantitative manner, we report here on the development of an automated high-resolution confocal RNAi screening platform in conjunction with advanced 3D image analysis. With this approach we were able to reliably detect the occurrence of APBs as colocalizations of PML and the telomere repeat binding factor 2 (TRF2) and to evaluate the effect of RNAi-mediated protein knockdown of nine different genes on their formation. The proteins identified in this manner represent potential targets for the development of drugs against tumors employing the ALT pathway.

2 Materials and methods

2.1 Cell culture

Human U2OS and HeLa cells (both ATCC) were cultured in DMEM and RPMI medium (GIBCO), respectively, containing 10% FBS (PAA) and 2 mM L-Glutamine (PAA). For the screening application, 100 000 cells were seeded per slide on Lab-Tek chambered coverglasses (Thermo Scientific) and incubated for 72 h to ensure an optimal cell density of 4–8 cells per acquired image. Transient transfection and generation of the stable cell line was performed as previously described [17]. The constructs for GFP-PML-III and TagRFP-TRF2 have been previously described [17]. The GFP-PML-IV, GFP-PML-V, and GFP-PML-VI constructs were kindly provided by Peter Hemmerich [18]. For immunofluorescence analysis, cells were fixed with 4% paraformaldehyde in PBS for 12 min and permeabilized for 5 min with 0.1% Triton X-100 in PBS. Immunostaining of fixed cells was conducted with a mouse anti-TRF2 antibody (1 h, 1:100, 4A794, Calbiochem) and a rabbit anti-PML antibody (30 min, 1:50, #sc-5621, Santa Cruz Biotechnology) in 10% goat serum in PBS. Visualization was conducted with an Alexa488-conjugated goat anti-rabbit antibody (1:300, Molecular Probes) and an Alexa568-conjugated goat anti-mouse antibody (1:300, Molecular Probes) for 1 h in 10% goat serum in PBS. Cells were mounted with ProLong Gold (Invitrogen) containing 4′,6-diamidino-2′-phenylindole (DAPI). For fluorescence activated cell sorting (FACS) analysis, U2OS cells were fixed with 70% Ethanol and kept on ice for 2 h. After washing with PBS, cells were suspended in PBS containing 0.25 μM TO-PRO3 and 50 μg/mL RNase I. DNA content of 50 000 cells was measured using a FACSCalibur instrument.

2.2 RNA interference

The following siRNAs (silencer select siRNAs, Ambion) were used: 5′-AAGCCAGGTTCTAGAGGATG

ATT-3′ (53BP1, [19]), 5′-CTCTGGTATGGACACAG CT-3′ (MMS21, [15]), 5′-CGACAGCCCAGAAGAGG AA-3′ (PML, [20]); for 5′-CCATGGAATCCAAATTA AT-3′ (Sp100, [16]), 5′-GAATATTTGGTGATCCAA A-3′ (TRF1, [21]), 5′-GCAATTGTCATAAAACCAA-3′ (ATM), 5′-GGAAGAGTGTTCTATCTCA-3′ (Rad17), 5′-CAAGAAACTCAAAGAATCA-3′ (SUMO1), 5′-CATCCTGACTACTACCGTA-3′ (SUMO2), 5′-AGG CAGGGCTTGTCAATGA-3′ (SUMO3), and 5′-CCACCATTATTTCACCCGA-3′ (Ubc9). For all siRNAs used here, knockdown of protein expression was confirmed with western blots. Non-targeting controls were purchased from Ambion (silencer select negative control #1 and #2). Transfected cell microarrays were produced as previously described [4]. Repetitions of a 4×4 array were printed on each Lab-Tek resulting in 384 spots with 24 replicates for each siRNA. For manual RNAi studies, U2OS cells were seeded 1 day before transfecting them with 100 nM siRNA using Lipofectamine 2000 according to the manufacturer's instructions (Invitrogen). After 48 or 72 h, cells were either immunostained or harvested for western blotting.

2.3 Western blotting

Cells were lysed with RIPA buffer (150 mM NaCl, 1% NP40, 0.5% Na-Desoxycholate, 0.1% SDS, 50 mM Tris pH = 8.0, complete protease inhibitor cocktail (Roche Applied Science)) for 30 min at –80 °C. Cell lysates were electrophoretically separated on SDS-PAGE gels and electrotransferred to a nitrocellulose membrane. Proteins were detected with the following antibodies: mouse anti-Actin (1:1000, #ab8226, Abcam); rabbit anti-MMS21 (1:2000, #PAB1071, Abnova); rabbit anti-PML (1:200, #sc-5621), rabbit anti-Rad17 (1:200, #sc-5613) both Santa Cruz Biotechnology. Secondary antibodies: HRP-linked anti-mouse IgG (1:2000), HRP-linked anti-rabbit IgG (1:2000) (Cell Signaling). Blots were imaged using the INTAS ChemoCam Imager with a 16 bit camera.

2.4 Fluorescence microscopy

Confocal fluorescence images were acquired with a Leica TCS SP5 DMI6000 confocal laser scanning microscope (oil immersion objective lens, 63×, 1.4 NA). Three laser sources were used for excitation with wavelengths of 405 nm (DAPI), 488 nm (Alexa488), and 561 nm (Alexa568) at laser intensities in the range of 1–15 mW and corresponding acquisition of fluorescence with photomultipliers at 420–460, 500–540, and 580–650 nm. Parameters were chosen to avoid signal saturation. For the screening application the Matrix Screener software (Leica Microsystems) was used. Focus maps were created prior to screening with a noise-based autofocus method implemented in the Matrix Screener software to determine the z-position of the cells. For autofocusing, images of the DAPI channel were acquired 50 µm along the *z*-axis with a step size of 1 µm, a sampling rate of 600 Hz and a resolution of 64×64 pixels. During screening, images were taken in a sequential mode with a sampling rate of 500 Hz, a resolution of 512×512 pixel, a 3× zoom, a bit depth of 8 and a pinhole size of 1 Airy disk. Optical sections had a spacing of 250 nm and were recorded for 10 µm along the *z*-axis. These parameters ensured that the entire cell was covered at a resolution sufficient for reliably detecting the relatively small telomeres and colocalizations in 3D. The pixel dwell time was ~4 µs, yielding 2 image frames per second and a whole 3D three-color image stack in about 70 s. After every 16th 3D three-color image stack, the focus map was adapted with the autofocus procedure to compensate for stage drifts. For widefield microscopy an inverted Olympus IX81 microscope with a 60×/1.3 NA oil immersion objective was used. The Huygens software from Scientific Volume Imaging was employed for deconvolution. Chromatic aberrations were measured with "TetraSpeck" fluorescent beads (Invitrogen). The manual analysis of microscopy images was done with the ImageJ software (http://rsbweb.nih.gov/ij).

2.5 Automated image analysis

The automated image analysis was performed using a 3D model-based segmentation approach [22]. Performance of the software was tested by comparing the results of the automated image analysis with manual analysis and different intensity correlation-based schemes (Pearson's correlation coefficient and Manders colocalization coefficients) [22]. Here, the results of the automatic image evaluation were always checked by visual inspection of random samples. For segmenting telomeres and PML nuclear bodies, we used a SD of $\sigma = 1.1$ for Gaussian smoothing and a size of $5 \times 5 \times 5$ voxel for local maxima search. For segmenting cell nuclei, we used a SD of $\sigma = 1.2$ for Gaussian smoothing, Otsu thresholding with two thresholds, and a radius of 2 voxel for morphological opening. Analysis was performed on a Hewlett-Packard scalable visualization array computer system consisting of 10 nodes with 128 cores. Cells were excluded from the analysis if (i) not the entire cell was recorded, i.e. >300 voxel were at the border of the image in *xy*-direction (43.2% of the cells), (ii) the cell volume exceeded 370 000 voxel as compared to normal cells

with 50 000 to 120 000 voxel (0.2%), or (iii) less than 15 telomeres were detected (8.8%). For the cell cycle analysis, a histogram of the background-corrected integrated DAPI intensity was fitted with two Gaussians for the G1 and the G2 peaks. The intensity in the middle between the means was used as a threshold to separate the cell cycle phases. The image analysis software is available from the authors on a collaborative basis.

2.6 Statistical analysis

The statistical analysis was carried out with the R software (http://www.r-project.org/). The following routines were used: for the two-sample t-test, t.test (package: stats); for the rate ratio test, rateratio.test (package: rateratio.test); for the Wilcoxon test, wilcox.test (package: stats). For the Kolmogorov-Smirnov (KS) test the maximum of the difference between the two empirical distribution functions is $D_{n,n'} = \sup_x |F_{1,n}(x) - F_{2,n'}(x)|$, where n and n' are the number of observations of the first and the second sample, respectively. The null hypothesis was rejected at level α if $L_x < K_\alpha$, where L_x is the limiting cumulative distribution function of $\sqrt{\frac{nn'}{n+n'}} D_{n,n'}$. The values of K_α were chosen according to ref. [23].

3 Results and discussion

To identify proteins that are required for the formation of APBs, we developed a high-resolution confocal RNAi screen in conjunction with an advanced image analysis approach. We configured a Leica TCS SP5 microscope with an integrated matrix screener for automated high-content confocal screening based on the setup described previously [8]. With this approach we were able to acquire 3D image stacks at high-throughput to reliably resolve APB structures in their nuclear context.

3.1 Visualization of proteins for colocalization studies

Different labeling techniques to identify APBs by the colocalization of PML and the telomere binding protein TRF2 were evaluated according to the following criteria: (i) a high labeling efficiency, (ii) suitability for high-throughput experiments, and (iii) a homogenous fluorescence signal with low background. Transient transfection of U2OS cells with plasmids expressing GFP/RFP fusion proteins of PML or TRF2 resulted in a low number of co-transfected cells (Fig. 1A). In addition, overexpression led to heterogeneous expression levels of TRF2 and the formation of PML aggregates due to PML's self-assembly properties. To overcome the problem of low transfection efficiency, a stable cell line overexpressing the GFP-PML-III splice variant was generated. Transient transfection of this cell line with a plasmid expressing TagRFP-TRF2 yielded more cells suitable for colocalization analysis (Fig. 1B). However, additional siRNA transfection as well as stable overexpression of TagRFP-TRF2 resulted in increased apoptosis (data not shown). Furthermore, transfection with different PML isoforms was found to perturb the equilibrium of endogenous proteins as inferred from a comparison with immunostaining (Fig. 1D). Overexpression of PML isoforms III, V, and VI yielded a reduced number of APBs, whereas PML IV overexpression resulted in an increase. This could be related to the direct interaction of PML IV with the telomere repeat binding factor TRF1 supposedly promoting APB formation [24]. We suspect that overexpression of other PML isoforms downregulates expression of endogenous PML protein, thus reducing the amount of the telomere-binding PML IV isoform. Hence, introduction of exogenous PML protein is clearly inappropriate in our system, since this changes the number of APB complexes, which is the central experimental observable of our screen. Accordingly, immunofluorescence labeling was tested. This resulted in an even labeling of all cells without additional cell stress (Fig. 1C). Furthermore, the fluorescent probes used were less sensitive to photobleaching and allowed a better spectral separation of the fluorescence emission signals than the autofluorescent GFP and RFP domains. Therefore, immunofluorescence was used for protein visualization in the confocal RNAi screen.

3.2 Manual assessment of controls as quality reference for the setup of the RNAi screen

To be able to assess the quality of the confocal RNAi screen, different references were established by manual knockdown experiments (Fig. 2, Supporting information, Fig. S1). The goal was to assure that the automatic RNAi screen would yield similar results with respect to the knockdown effects as those obtained from visual inspection of the cells. We investigated proteins known to be involved in APB formation (PML [16, 24], TRF1 [16], and MMS21 [15], a E3 SUMO ligase) as well as proteins that have been shown to have no significant effect on APB formation (Sp100 [16], 53BP1 [16], ATM [25]). Additionally, a protein that co-localizes with

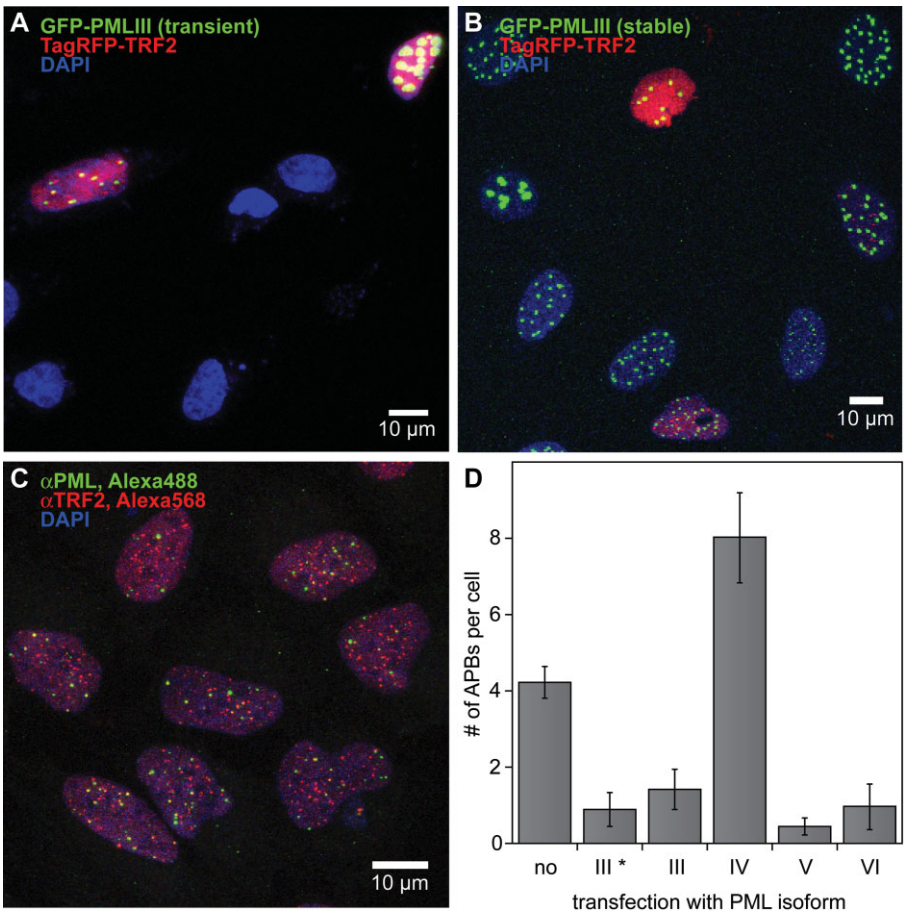

Figure 1. Comparison of various techniques for the visualization of telomeres and PML-NBs. (**A**) The U2OS cell line was transiently co-transfected with GFP-PML-III and TagRFP-TRF2 expression vectors. (**B**) Transient transfection of a U2OS cell line stably expressing GFP-PML-III with a TagRFP-TRF2 expression vector. (**C**) U2OS cells were immunostained with antibodies directed against PML and TRF2. (**D**) Changes in the average number of APBs per cell compared to the non-transfected immunostained control as a result of transient overexpression of different PML isoforms. Stable expression of PML-III (marked by *) suppressed the formation of APBs. Cells were analyzed 63 h post transfection. Error bars show SEM.

APBs (Rad17 [25]) and other proteins potentially involved in APB formation were tested (isoforms 1, 2, and 3 of the small ubiquitin-like modifier (SUMO) and Ubc9, the E2 SUMO ligase). The efficiency of gene knockdown was evaluated by western blotting and the effect on APB formation was analyzed by manually counting colocalizations between telomeres and PML nuclear bodies (PML-NBs). As an example for a strong positive control, knockdown of PML is shown in Fig. 2A. MMS21 represents a protein with a significant effect on APB formation (Fig. 2B). As an assay-specific negative control, the knockdown of Rad17 is presented in Fig. 2C. Rad17 is colocalizing with APBs [25] but has no apparent effect on APB formation (Fig. 2C). To test for sequence-independent off-target effects of the siRNA transfection procedure, e.g., due to interferon response, we analyzed the influence of a non-targeting negative control (scrambled siRNA) on APB formation (Fig. 2D). A significant decrease in the number of APBs was observed when transfecting the control #1. Reduction of the concentration of the siRNA to 10 nM gave the same result suggesting a sequence-specific effect. This could be confirmed by transfecting another non-targeting control #2, where no significant change was detected.

3.3 Microscope setup for 3D colocalization studies

For the 3D colocalization studies of telomeres and PML-NBs different imaging systems were compared in order to optimize the identification of colocalizations. Widefield microscopy is commonly used for high-throughput RNAi screens [5]. Therefore, images were acquired with a widefield fluorescence microscope to assess whether the image quality was sufficient for 3D colocalization studies. The resulting images showed a high amount of out-of-focus light and a low contrast that decreased detection efficiency especially for small telomeres (Fig. 3, first row). Due to the lack of z-resolution, PML-NB and telomeres were detected as false-positive colocalizations even if they were separated in *z*-direction. The images were deconvolved to suppress out-of-focus light and to enhance the contrast (Fig. 3, third row). This significantly improved the image quality. However, deconvolution

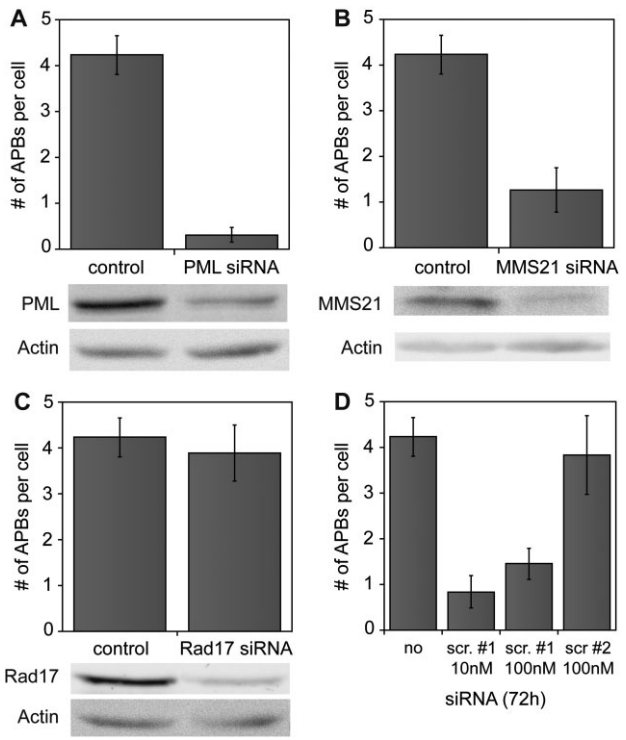

Figure 2. Manual assessment of the effect of various siRNAs on APB appearance. (**A**) PML as a strong positive control to inhibit APB formation. The knockdown efficiency of the transfection with PML siRNA was analyzed by western blotting. (**B**) Transfection with an siRNA targeting MMS21 resulted in a reduction of MMS21 protein level and the average number of APBs per cell. (**C**) Assay-specific negative control: RNAi-mediated knockdown of Rad17. (**D**) Transfection with a non-targeting control siRNA (scrambled #1) led to a significant decrease in the number of APBs per cell. A similar behavior was seen after the transfection with a lower concentration of the siRNA (10 nM). The transfection of another non-targeting siRNA (scr. #2) showed that the reduction caused by scr. #1 was likely due to sequence-dependent targeting. Error bars show SEM.

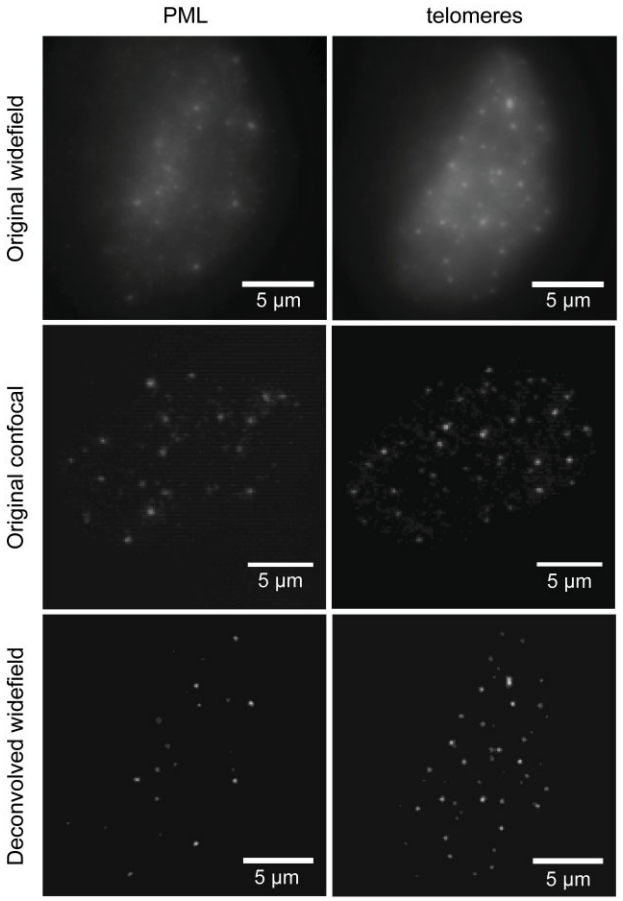

Figure 3. Evaluation of different image acquisition systems. Image acquisition with a widefield microscope resulted in out-of-focus light and a low contrast that led to false identification of colocalizations of telomeres and PML-NBs (first row). The original confocal image (second row) show significantly less blurring and out-of-focus light and improved the detection of colocalizations. The deconvolved widefield image (third row) is comparable in terms of quality to the original confocal image but, depending on the image and the deconvolution settings, artifacts may be introduced. All images are average intensity projections.

represents an additional computational-intensive image-processing step and cannot substitute for true optical sectioning along the optical axis. In addition, it can introduce artifacts. Best results were obtained when images were acquired with a confocal microscope where no further image processing was required (Fig. 3, second row). The overall image quality was similar to the deconvolved widefield images. However, the better contrast in the raw confocal images in conjunction with the improved optical sectioning led to a more sensitive detection of small telomeres, which were partially removed by deconvolution due to background suppression. Image acquisition times for widefield and confocal microscopy were found to be similar when adapting parameters like scan speed and resolution to the demands of automatic image analysis (see *Materials and methods*). Considering the additional deconvolution step required for the widefield analysis and the improved 3D resolution, the confocal image acquisition was found to be advantageous. Accordingly, the screen was performed with a confocal laser scanning microscope. For this system the chromatic shift between the two channels used for colocalization analysis was measured with 100 nm beads stained with four different fluorescent dyes. The chromatic shift was smaller than 50 nm in all directions for emission at 500–540 and 580–650 nm. The shift could be neglected for the analysis since it was well below the optical resolution of the microscope. However, when using red labels with emission in the far red the chromatic shift between the green and red channel became significant and a value of 100 nm in *xy*-direction and 200 nm in *z*-direction was measured at 645–700 nm detection.

3.4 Detection of colocalizations via automated image analysis

To automatically quantify the number and volume of telomeres, PML-NBs and APBs of individual cell nuclei in three-channel 3D image stacks, we developed a 3D model-based segmentation approach (Fig. 4, 5A). To segment the cell nuclei in the DAPI channel, we applied a 3D Gaussian filter for noise reduction with subsequent Otsu thresholding and morphological operations (hole filling and opening) (Fig. 4F). Since cell nuclei often touch each other, a 3D labeling approach was developed to split touching nuclei. This approach exploits concavities of the contour and is based on morphological operations (e.g., erosion). A three-step procedure was used for the telomere and PML-NB channels: First, different 3D image analysis operations were applied to the image stacks to obtain coarse center positions for the different spots [22, 26, 27]. These operations include 3D Gaussian smoothing for noise reduction, intensity clipping with automatically computed threshold values for background suppression, and local maxima search within cubic 3D regions-of-interest (ROIs) for spot detection (Fig. 4D, E). In the second step, each detected spot candidate obtained in the first step was quantified using 3D model fitting [22]. For telomeres and PML-NBs the 3D intensity profile can be well represented by a 3D Gaussian function (Fig. 4G, H). Therefore, we modeled these structures using a parametric 3D Gaussian intensity model. The image structures were quantified using least-squares fitting of the model to the image intensities

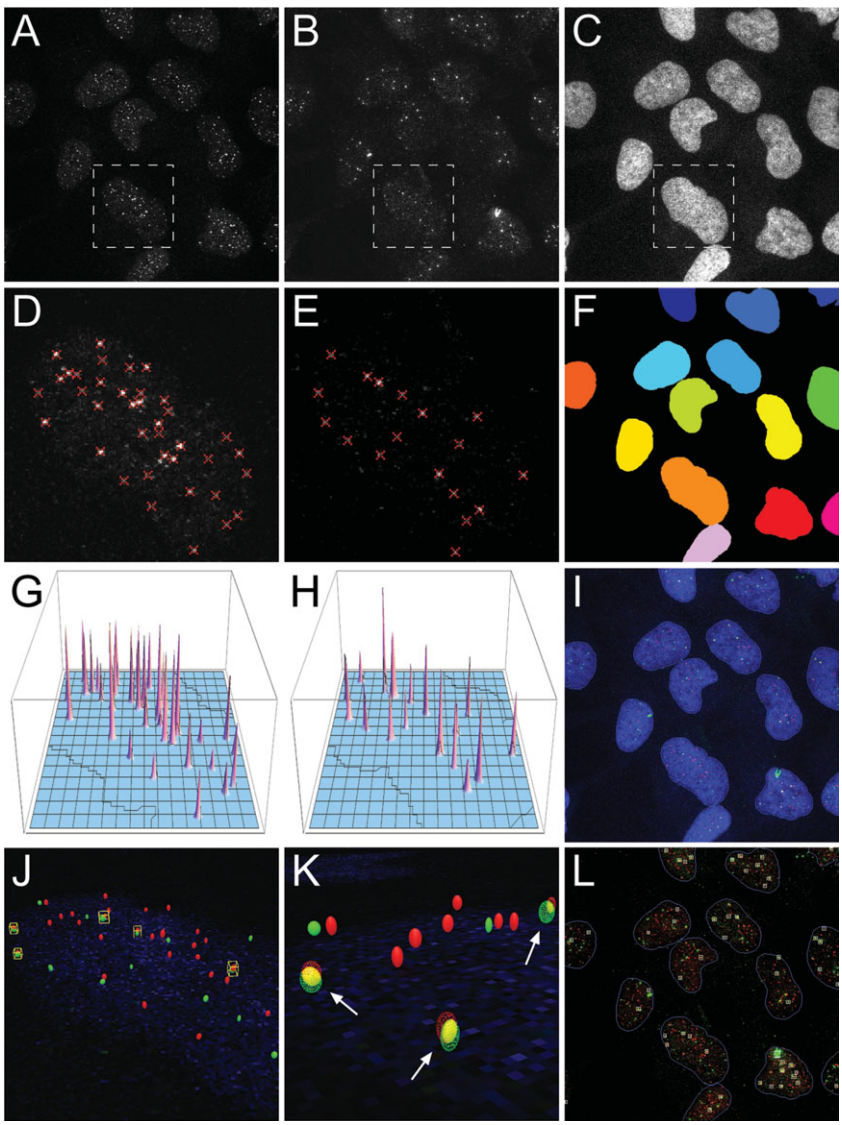

Figure 4. Automatic image analysis using a 3D model-based approach. (**A**, **B**) Colocalization candidates were detected in the telomere and PML-NB channels and were subsequently quantified using 3D model fitting with parametric intensity models. The results of both channels were combined for 3D geometry-based colocalization analysis. A region-of-interest (ROI) of one cell is indicated. (**C**) In the DAPI channel, the cell nuclei were segmented and labeled in 3D. The cell cycle state for single nuclei was determined based on the integrated intensity. (**D**, **E**) Local intensity maxima represent colocalization candidates (marked by crosses) within the ROI of telomere and PML-NB channel, respectively. (**F**) Segmented and labeled cell nuclei in the DAPI channel. (**G**, **H**) 3D intensity plots for telomeres and PML-NBs, respectively, identified within the ROI. (**I**) Overlay of telomere, PML-NB and DAPI channels with contours of the segmented cell nuclei. (**J**, **K**) 3D visualization of colocalizations indicated by bounding boxes and arrows. (**L**) Overlay of telomere and PML-NB channels with contours of segmented cell nuclei and bounding boxes marking colocalizations. All CLSM images are maximum intensity projections.

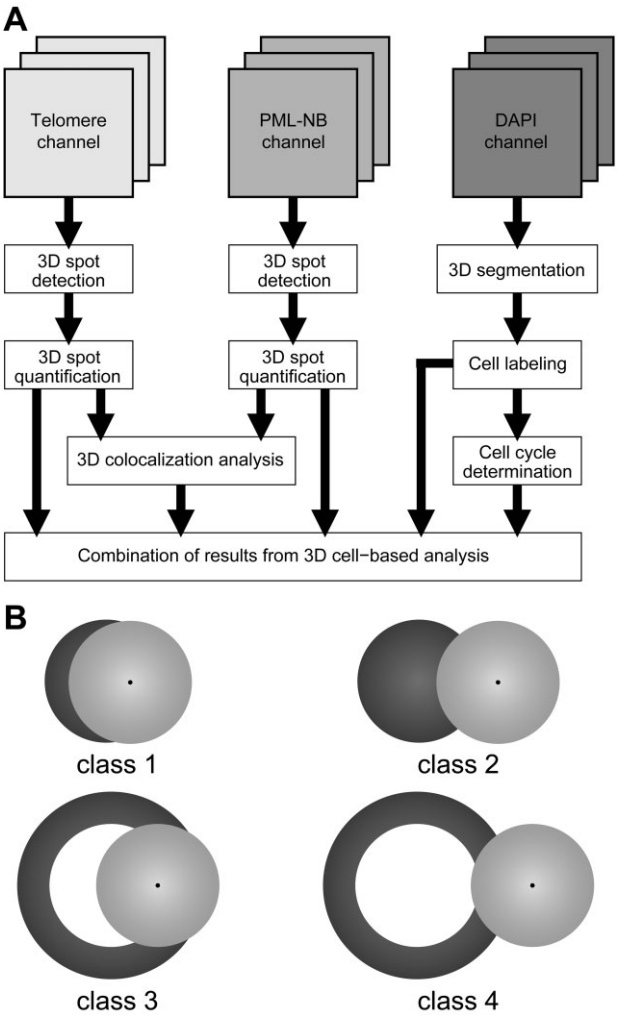

Figure 5. Automatic detection of APBs. (**A**) Workflow of the automatic image analysis using a 3D model-based segmentation approach. (**B**) Illustration of the different classes of colocalizations of telomeres (light gray) and PML-NBs (dark gray): class 1, center of the telomere lies within the volume of the PML-NB; class 2, telomere and PML-NB partially overlap. Class 3 and 4 are equivalent to class 1 and 2 for large PML-NBs, respectively, which appear as hollow spheres. The number of unambiguous APBs is computed from the sum of class 1 and 3, while the total number of PML-NB colocalizations with telomeres is the sum of all classes (1 to 4).

within 3D ROIs. Based on the model fitting results, we obtained a 3D geometric representation for each spot. In the last step, colocalizations between telomeres and PML-NBs were determined (Fig. 4J–L). Here, the geometry of the subcellular structures based on the fitting results of the second step was exploited. The geometry of the spots is given by their 3D position, orientation and shape (specified by the standard deviation of the 3D Gaussian), which were determined with subvoxel resolution. Here, we defined four different types of colocalizations (Fig. 5B): class 1 is a colocalization where the center of a telomere spot lies within a PML-NB spot, and class 2 is a colocalization where a telomere spot partly overlaps with a PML-NB spot. Large APBs, where PML-NBs appear as hollow spheres, were classified as class 3 and 4 (equivalent to class 1 and 2 for large APBs). For the statistical evaluation four different parameters were quantified: (i) Colocalizations of PML-NBs and telomeres as given by the sum of complexes in class 1 and 3. Based on our previous structural analysis of the APB structure, we consider these as unambiguously identified APBs. In these APBs the PML protein forms a cap-like structure that surrounds the telomere repeat [13]. (ii) The number of all PML-NB and telomere colocalizations per cell (sum of class 1–4) yielding a less stringently defined group of APBs. This also includes complexes that display only a partial overlap of the PML and telomere signal according to the classification scheme in Fig. 5B. (iii) The total number of telomeres, and (iv) the total number of PML-NBs.

3.5 Characterization of the ALT-positive U2OS cell line

Previous studies reported contradictory results concerning the number and size of APBs [25, 28–30]. Accordingly, an unbiased analysis of U2OS cells using our automatic image analysis approach was performed. The telomerase-positive and ALT-negative HeLa cell line was used as a control for assessing the occurrence of false-positive colocalizations because these cells do not contain APBs. The number and size of APBs, PML-NBs, and telomeres in U2OS cells were evaluated as described above (Fig. 6C, D). One or more APBs (class 1–4) could be detected in over 90% of the U2OS cells with an average of 4.4 ± 0.1 APBs per cell (Fig. 6A). In contrast, the ALT-negative HeLa cell line displayed an average of 0.5 ± 0.1 colocalizations per cell and only $34 \pm 5\%$ cells with colocalizations (Fig. 6B). Thus, the apparent upper limit for the error rate can be estimated to be around 10% when comparing the average number of APBs of 4.4 ± 0.1 in U2OS cells to that of 0.5 ± 0.1 in the HeLa cell line. The latter value reflects random superposition of the two signals, the limits in resolution of the microscope as well as background noise of the immunofluorescence. Additionally, a transient telomere association of PML-NBs occurs also in non-ALT cell lines after PML-NB disassembly in mitosis so that some genuine complexes of PML and telomeres are likely to be present also in HeLa cells [31, 32]. In U2OS cells the PML volume within APBs (class 1 + 3) was larger than that of free PML-NBs, most likely because of the additional

space occupied by the telomeric repeats (Fig. 6E). Interestingly, telomeric sequences located within APBs were found to occupy a larger volume compared to free telomeres ($0.0202 \pm 2 \cdot 10^{-4}$ μm^3 vs. $0.0150 \pm 1 \times 10^{-4}$ μm^3) (Fig. 6F). This could reflect the induction of telomere extension by the APB complex, an increased probability of PML to associate with long telomeres, or the clustering of two or more telomeres inside an APB, which has been proposed to facilitate recombination [33].

3.6 Analysis of cell cycle dependency of APB appearance

Cell cycle studies of APBs suggest that they accumulate in late S/G2 phase [34, 35]. However, a recent study indicates that APB formation could be induced by cell cycle blocking agents [36]. To analyze the cell cycle dependencies of APB appearance without a potentially perturbing synchronization, the cell cycle state was determined by measuring the DAPI signal of the cells to obtain their DNA content. The histogram of the background-corrected integrated DAPI intensity of the cells was compared with the FACS cell cycle analysis of equally treated cells (Fig. 7A). A good correlation of the DNA content of the cells analyzed by microscopy and FACS was obtained. Analysis of the appearance of APBs (class 1–4) revealed that cells in S/G2 phase seem to contain slightly more APBs than cells in G1 phase (G1: 4.0 ± 0.1 APBs per cell, S/G2: 5.5 ± 0.3 APBs per cell) (Fig. 7B). This could simply reflect the increase of the number of PML-NBs after disassembly in mitosis [31] (Fig. 7C) and the replication of telomeres during the S phase. Indeed, the histograms of APBs in G1 and S/G2 phase normalized to the number of PML-NBs and telomeres per cell showed the opposite trend, i.e. cells in G1 phase contained slightly more APBs than in S/G2 (data not shown). Thus, we conclude that there is no or only a very weak correlation of APB appearance with the cell cycle.

3.7 Statistical analysis of the RNAi screen

For the automated confocal screen cells were transfected by seeding them on microarrays with 384 siRNA spots. Cells were immunostained after 48 or 72 h incubation and four images of every spot with a diameter of 400 μm were automatically acquired. This resulted in 1 500 high-resolution 3D image stacks containing 260 000 images per slide and around 2.1 million images in total for the study presented here. For the 72 h time point four biological replicates were automatically analyzed (i.e., separate biological samples that were treated using the same protocol) and two replicates for the 48 h time point. The replicates were analyzed separately (Supporting information, Table S2) and combined (Supporting information, Table S1).

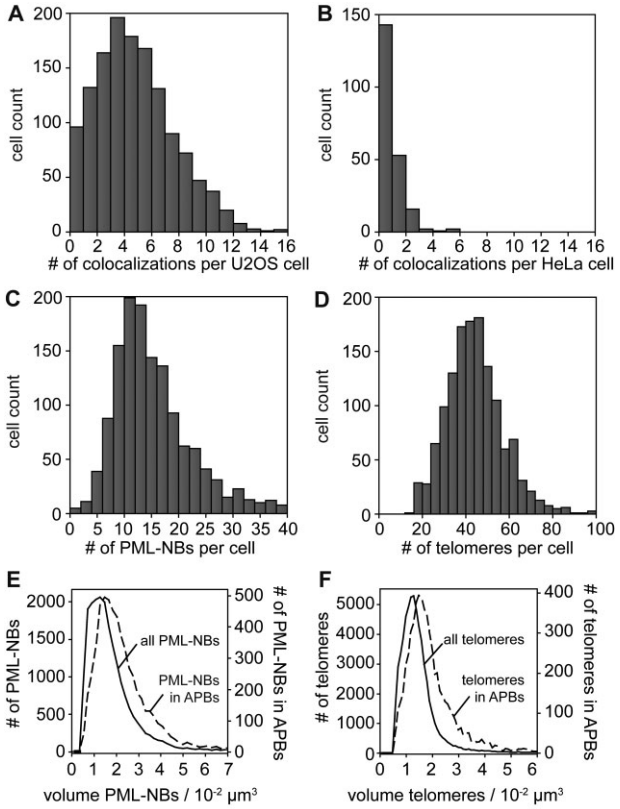

Figure 6. Analysis of the ALT-positive U2OS cell line and the telomerase-positive HeLa cell line. (**A**) Histogram of the number of colocalizations in the ALT-positive U2OS cell line (n = 1351 cells). (**B**) Analysis of the ALT-negative and telomerase-positive HeLa cell line. (**C**) Histogram of the number of PML-NBs per U2OS cell yielded an average number of 15.1 ± 0.2 PML-NBs. (**D**) Histogram of the number of telomeres in U2OS cells. An average of 44.1 ± 0.4 telomeres per cell were detected. (**E**) Comparison of the size distribution of all PML-NBs in U2OS cells (left *y*-axis) with PML-NBs that colocalize with telomeres (PML-NBs in APBs, right *y*-axis). PML-NBs-containing telomeres have an average volume of $0.0266 \pm 3 \times 10^{-4}$ μm^3 compared to normal PML-NBs with $0.0198 \pm 1 \times 10^{-4}$ μm^3. (**F**) Volume of telomeres in APBs (right *y*-axis) and normal telomeres (left *y*-axis).

The effect of gene knockdown was evaluated in terms of (i) unambiguously identified APBs (class 1 + 3, Fig. 5B), (ii) the number of all APB-like colocalizations of PML-NBs and telomeres (sum of class 1–4), (iii) the total number of telomeres, and (iv) the total number of PML-NBs. Different statistical significance tests were applied to account for deviations from the normal distribution (Fig. 6A, C). In these cases non-parametric statistical tests should be used, e.g., rank-based tests as the Wilcoxon or Mann–Whitney U-test. However, due to the presence of ties in the data (i.e., repetitions

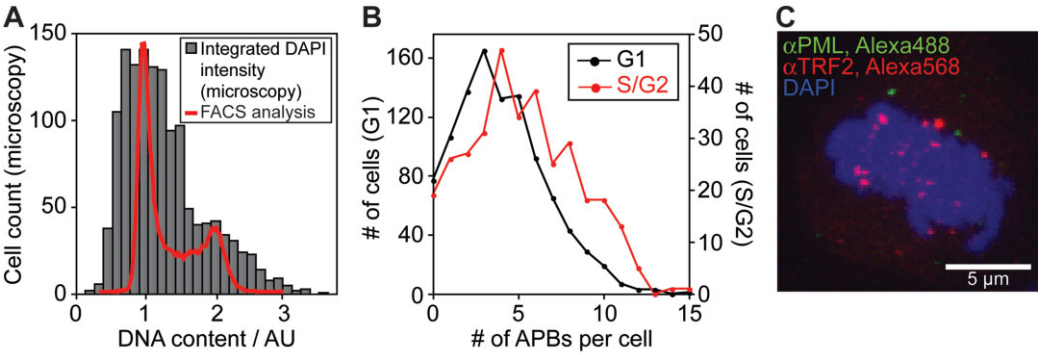

Figure 7. Analysis of the cell cycle dependency of APBs. (**A**) Histogram of the integrated background-corrected DAPI intensities together with the FACS cell cycle analysis of similar treated cells (solid line). (**B**) Histogram of the number of APBs in G1 or S/G2 phase. The value of 8.3×10^6 for the integrated DAPI intensity (equivalent to 1.5 genomes) was used to separate between G1 and S/G2 phase. 1351 cells were analyzed. (**C**) Maximum intensity projection of a metaphase cell stained with antibodies against PML and TRF2.

of the same value) these tests can only calculate approximate *p*-values. Although the counting data were expected to be Poisson-distributed, analysis with Pearson's chi-square test revealed a clear deviation from this type of distribution. This could reflect heterogeneity of the samples, e.g., the superposition of different Poisson distributions. Four statistical tests were compared: the *t*-test for a normal distribution, the rate ratio test for Poisson distributions, the Wilcoxon or Mann–Whitney U-test as a non-parametric rank-based test and the KS test as another non-parametric test without the use of ranks (Supporting information, Table S1 and S2). The results were evaluated with respect to the conclusions drawn from the manual data analysis for different siRNAs (Fig. 2 and 8, Table 1). The

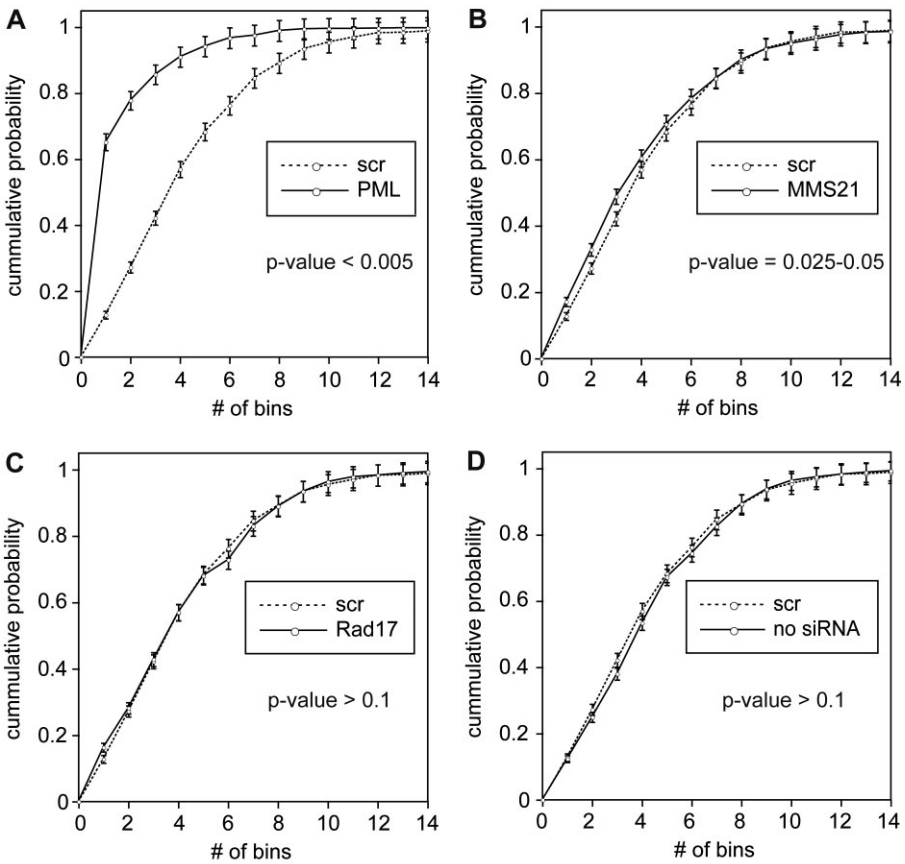

Figure 8. The KS test was used to evaluate the effect of gene knockdown on different parameters. All error bars show the counting error (√n). (**A**) Treatment with PML siRNA vs. non-targeting scrambled siRNA (scr). The knockdown of PML significantly reduced the number of APBs per cell ($p < 0.001$). (**B**) Effect of knockdown of MMS21 on the number of APBs per cell (*p*-value between 0.025 and 0.05). (**C**) Effect of Rad17 knockdown on the number of colocalizations per cell. (**D**) Comparison of the non-treated control with the control treated with non-targeting siRNA.

Table 1. Changes of the number of APBs, telomeres, and PML-NBs observed in response to RNAi-mediated knockdown at different time points (48 h/72 h)[a)]

siRNA	unambiguous APBs (class 1 + 3)	all APBs (class 1–4)	PML-NBs	telomeres
no siRNA	n.s./n.s.	n.s./n.s.	n.s./n.s.	n.s./n.s.
53BP1	n.s./n.s.	−−/− −15 ± 2%	−−/−− −24 ± 2%	n.s./n.s.
ATM	n.s./n.s.	−/n.s. −14 ± 4%	−/− −17 ± 2%	n.s./n.s.
MMS21	−−/−− −37 ± 4%	−−/− −7 ± 2%	n.s./n.s.	+/+ +8 ± 1%
PML	−−/−− −81 ± 1%	−−/−− −74 ± 2%	−−/−− −67 ± 1%	n.s./n.s.
Rad17	n.s./n.s.	n.s./n.s.	n.s./n.s.	n.s./n.s.
Sp100	n.s./n.s.	n.s./n.s.	−/n.s. −15 ± 2%	n.s./n.s.
SUMO 1/2/3	−−/−− −41 ± 4%	−−/−− −31 ± 2%	−−/−− −35 ± 2%	n.s./n.s.
TRF1	n.s./++ +22 ± 5%	n.s./+ +13 ± 3%	n.s./n.s.	−−/−− −21 ± 1%
Ubc9	−−/−− −49 ± 2%	−/−− −40 ± 2%	−−/−− −26 ± 1%	n.s./n.s.

a) The effect of RNAi-mediated knockdown on the number of APBs, PML-NBs, and telomeres after 48 and 72 h was analyzed and evaluated with a two-sided KS test as described in the text. The results were classified as ++, highly significant increase (p-value <0.005); +, significant increase (p-value <0.05); n.s., difference not significant; −, significant decrease (p-value <0.05); −−, highly significant decrease (p-value <0.005). The results from the significance test are shown for both time points (48 h/72 h). In addition, the percentage of the largest decrease/increase compared to treatment with scrambled siRNA is given. For the 72 h time point four replicates (at least 668 cells per siRNA) were analyzed and two for the 48 h time point (at least 214 cells per siRNA).

best agreement was found for the self-implemented KS-test (see *Materials and methods*) with regard to the change of the distributions upon gene knockdown. The test is very robust and can be applied without any assumption of the underlying distribution. Similar results were obtained by using the KS-test implemented in the R software (ks.test) but with slightly deviating results for APBs of class 1 and 3. To obtain a high stringency, we choose the self-implemented KS-test that yielded less false-positive hits.

3.8 Biological significance of results from RNAi-mediated protein knockdown

Our screen included nine different proteins, which have diverse functions in the cell. While this is only a small number of proteins, the large number of cells evaluated by a high-resolution 3D image analysis in an unbiased manner provides valuable insight into the mechanisms that control APB formation. As reported previously, PML sumoylation is necessary for PML-NB formation [37, 38], and many proteins in canonical PML-NBs and APBs are sumoylated or contain a SUMO interaction motif. In addition, components of the shelterin complex such as TRF1, TRF2, and Rap1 become sumoylated through the MMS21 E3 SUMO ligase, which is required for APB formation [15]. Therefore, MMS21, three SUMO isoforms and Ubc9, the E2 SUMO ligase, were included in our study. Knockdown of these proteins resulted in a significant reduction of APBs with SUMO and Ubc9 being also needed for PML-NB formation (Table 1). While the role of SUMO and Ubc9 in PML-NB formation has been described previously, we demonstrate here for the first time directly that they are required also for APB formation. For MMS21, the overall number of APBs decreased only slightly upon knockdown, while the decrease of the number of unambiguous APBs (class 1 + 3) was four to five-fold more pronounced (Table 1). In comparison, all other siRNAs showed only slight differences between the number of unambiguous and total APBs (between 1.2 and 1.8-fold). This strong decrease of unambiguous APBs supports one of two previously proposed models for the mode of action of MMS21 [15]: A yet unknown factor recruits PML-NBs to the close proximity of the telomeres, but MMS21-mediated sumoylation of the shelterin proteins is necessary for maintaining stable associations between PML-NBs and telomeres.

Several other proteins were investigated previously using the methionine restriction method to artificially increase the number of APBs: PML and TRF1 knockdown significantly impaired APB formation, whereas knockdown of 53BP1 and Sp100 showed no effect [16]. The results of PML and Sp100 knockdown could be confirmed with our screen (Table 1). However, after knockdown of TRF1 we detected a slight but significant induction of APB formation after 72 h and a reduced number of detectable telomeres. This suggests that the artificially introduced APBs might be different from the normally present endogenous APBs. Indeed, a recent report showed that after methionine restriction the majority of APBs lack the MUS81 endonuclease, which is present in normal APBs [39]. Furthermore, it was reported that transient siRNA-mediated knockdown of TRF2, another shelterin protein, yielded a slight increase of APBs [40]. However, the difference was not significant due to the low number of analyzed cells. Our screen allowed the analysis of around thousand cells for each siRNA with high spatial resolution so that relatively small differences could be reliably detected.

An inspection of the data of 53BP1 and ATM knockdown shows a decrease of the total number of APBs, whereas the number of unambiguous APBs (class 1 + 3) remained unchanged (Table 1). This suggests that the knockdown effect is indirect and might reflect the decreased number of PML-NBs. It would argue for a previously unknown involvement of ATM and 53BP1 in PML-NB formation. However, ATM and 53BP1 seem to be not directly involved in APB formation because no change in the number of unambiguous APBs could be detected. This confirms results obtained with caffeine inhibition of ATM [25] and conclusions made by Jiang et al. [16] on the requirement of 53BP1 for APB formation. The knockdown of Rad17, which has been previously described to colocalize with APBs [25], had no significant effect on APB formation (Table 1). This is in agreement with experiments on the *de novo* formation of APBs showing that Rad17 is not able to induce their formation but is recruited to existing APBs (I. Chung, H. Leonhardt & K. Rippe, personal communication).

The results from the automatic image analysis were in good agreement with the manually evaluated experiments (Table 1, Fig. 2, Supporting information, Fig. S1). In the latter, the effect of RNAi-mediated knockdown appeared to be more pronounced. This could be due to an increased siRNA delivery *via* the liquid phase transfection used in these experiments as compared to the solid phase transfection used for the screening application. Furthermore, in the manual experiments less cells were analyzed and a bias cannot be excluded.

4 Concluding remarks

Here, we have developed an automated three-color confocal RNAi screening platform that allows us to analyze the appearance of colocalizations between telomeres and PML-NBs in three dimensions for the investigation of the ALT mechanism. Our screen provides a wealth of reliable and reproducible information about the effect of RNAi-mediated knockdown of specific genes on the number and size of telomeres, PML-NBs, and APBs. These data are obtained by an advanced 3D image analysis for each individual cell and are related to the cell cycle state as determined by the DNA content. This combination of detailed information is crucial for dissecting the role of different proteins in the ALT mechanism. The automation of the screen allows an unbiased analysis of the effect of different gene knockdowns in a large number of cells without artificially increasing the number of APBs. To obtain high-resolution spatial information, we automatically acquired and analyzed over 2 million images for a relatively small number of proteins. In contrast, a typical genome-wide widefield screen of all human genes requires only about 0.5 million widefield fluorescence microscopy images. In the current study, extensive controls were used to establish the screening platform. These can be reduced to some extend for speed-up. From our study we conclude that three replicates of each Lab-Tek with 24 spots per siRNA are sufficient to ensure good statistics. Therefore, the time to acquire the images for one gene can be reduced from 34 h in the current study to 17 h to acquire about 36 000 images (=900 3D stacks). Currently, our automated setup for a confocal colocalization screen is extended to investigate several hundred siRNAs. Thus, a pre-selection of candidate genes will still be required in the near future, although higher throughput is possible with further development of a parallelized confocal image acquisition setup. This could involve the use of a spinning disk or line scanning microscope to speed up image acquisition by a factor of ~10 and/or the use of multiple instruments in parallel. In return, the complete spatial information of three different fluorescence signals of interest is obtained. From the comparison with a manual analysis and results in the literature, we conclude that our screen provides a reliable novel tool to identify ALT-related proteins that represent possible targets for cancer therapy. The methodological advancements made in our study can be

directly applied to investigations of other nuclear sub-compartments such as the nucleolus, Cajal bodies, or splicing speckles. Furthermore, the setup can also be used in drug discovery studies for small-molecule compound screens and to investigate complex spatial relations in 3D between different nuclear subcompartments. Thus, we anticipate that the automated confocal multi-color 3D imaging and colocalization screening platform introduced here will provide a significant advancement for HCS approaches in a number of application areas.

We are grateful to Inn Chung, Fabian Erdel, Jan-Phillipp Mallm, Daniel Parisotto, and Simone Braun for help and valuable discussions and Peter Hemmerich for providing plasmid vectors. The ViroQuant-CellNetworks RNAi screening facility is supported by the Federal Ministry of Education and Research (BMBF) funded FORSYS program ViroQuant (Project 0313923) and by CellNetworks-Cluster of Excellence (EXC81). Parts of the computational work were supported by the BMBF programs Services@MediGRID (grant 01IG07015G) and SysTec (project EpiSys). Sarah Osterwald has been supported by the Helmholtz International Graduate School for Cancer Research.

Frank Sieckmann is employed by Leica Microsystems. Other authors declared no conflict of interest.

5 References

[1] Taylor, D. L., Past, present, and future of high content screening and the field of cellomics. *Methods Mol. Biol.* 2007, *356*, 3–18.

[2] Pelkmans, L., Fava, E., Grabner, H., Hannus, M. et al., Genome-wide analysis of human kinases in clathrin- and caveolae/raft-mediated endocytosis. *Nature* 2005, *436*, 78–86.

[3] Erfle, H., Simpson, J. C., Bastiaens, P. I., Pepperkok, R., siRNA cell arrays for high-content screening microscopy. *BioTechniques* 2004, *37*, 454–458.

[4] Erfle, H., Neumann, B., Liebel, U., Rogers, P. et al., Reverse transfection on cell arrays for high content screening microscopy. *Nat. Protoc.* 2007, *2*, 392–399.

[5] Conrad, C., Gerlich, D. W., Automated microscopy for high-content RNAi screening. *J. Cell Biol.* 2010, *188*, 453–461.

[6] Pepperkok, R., Ellenberg, J., High-throughput fluorescence microscopy for systems biology. *Nat. Rev. Mol. Cell Biol.* 2006, *7*, 690–696.

[7] Krishnan, M. N., Ng, A., Sukumaran, B., Gilfoy, F. D. et al., RNA interference screen for human genes associated with West Nile virus infection. *Nature* 2008, *455*, 242–245.

[8] Neumann, B., Walter, T., Heriche, J. K., Bulkescher, J. et al., Phenotypic profiling of the human genome by time-lapse microscopy reveals cell division genes. *Nature* 2010, *464*, 721–727.

[9] Blackburn, E. H., Greider, C. W., Szostak, J. W., Telomeres and telomerase: The path from maize, Tetrahymena and yeast to human cancer and aging. *Nat. Med.* 2006, *12*, 1133–1138.

[10] Dunham, M. A., Neumann, A. A., Fasching, C. L., Reddel, R. R., Telomere maintenance by recombination in human cells. *Nat. Genet.* 2000, *26*, 447–450.

[11] Cesare, Reddel, Alternative lengthening of telomeres: Models, mechanisms and implications. *Nat. Rev. Genet.* 2010, *11*, 319–330.

[12] Villa, R., Folini, M., Lualdi, S., Veronese, S. et al., Inhibition of telomerase activity by a cell-penetrating peptide nucleic acid construct in human melanoma cells. *FEBS Lett.* 2000, *473*, 241–248.

[13] Lang, M., Jegou, T., Chung, I., Richter, K. et al., Three-dimensional organization of promyelocytic leukemia nuclear bodies. *J. Cell Sci.* 2010, *123*, 392–400.

[14] Jiang, W.-Q., Zhong, Z.-H., Henson, J. D., Neumann, A. A. et al., Suppression of alternative lengthening of telomeres by Sp100-mediated sequestration of the MRE11/RAD50/NBS1 complex. *Mol. Cell Biol.* 2005, *25*, 2708–2721.

[15] Potts, P. R., Yu, H., The SMC5/6 complex maintains telomere length in ALT cancer cells through SUMOylation of telomere-binding proteins. *Nat. Struct. Mol. Biol.* 2007, *14*, 581–590.

[16] Jiang, W.-Q., Zhong, Z.-H., Henson, J. D., Reddel, R. R., Identification of candidate alternative lengthening of telomeres genes by methionine restriction and RNA interference. *Oncogene* 2007, *26*, 4635–4647.

[17] Jegou, T., Chung, I., Heuvelman, G., Wachsmuth, M. et al., Dynamics of telomeres and promyelocytic leukemia nuclear bodies in a telomerase-negative human cell line. *Mol. Biol. Cell* 2009, *20*, 2070–2082.

[18] Weidtkamp-Peters, S., Lenser, T., Negorev, D., Gerstner, N. et al., Dynamics of component exchange at PML nuclear bodies. *J. Cell Sci.* 2008, *121*, 2731–2743.

[19] Goldberg, M., Stucki, M., Falck, J., D'Amours, D. et al., MDC1 is required for the intra-S-phase DNA damage checkpoint. *Nature* 2003, *421*, 952–956.

[20] Xu, Z. X., Timanova-Atanasova, A., Zhao, R. X., Chang, K. S., PML colocalizes with and stabilizes the DNA damage response protein TopBP1. *Mol. Cell Biol.* 2003, *23*, 4247–4256.

[21] Xu, L., Blackburn, E. H., Human Rif1 protein binds aberrant telomeres and aligns along anaphase midzone microtubules. *J. Cell Biol.* 2004, *167*, 819–830.

[22] Wörz, S., Sander, P., Pfannmöller, M., Rieker, R. J. et al., 3D Geometry-based quantification of colocalizations in multichannel 3D microscopy images of human soft tissue tumors. *IEEE Trans. Med. Imaging* 2010, *29*, 1474–1484.

[23] Smirnov, N., Table for estimating the goodness of fit of empirical distributions. *Ann. Math. Stat.* 1948, *19*, 279–281.

[24] Yu, J., Lan, J., Wang, C., Wu, Q. et al., PML3 interacts with TRF1 and is essential for ALT-associated PML bodies assembly in U2OS cells. *Cancer Lett.* 2009, *291*, 177–186.

[25] Nabetani, A., Yokoyama, O., Ishikawa, F., Localization of hRad9, hHus1, hRad1, and hRad17 and caffeine-sensitive DNA replication at the alternative lengthening of telomeres-associated promyelocytic leukemia body. *J. Biol. Chem.* 2004, *279*, 25849–25857.

[26] Wörz, S., Heinzer, S., Weiss, M., Rohr, K. in: Hu, X. P., Clough, A. V. (Ed.), *Proc. SPIE Medical Imaging 2008: Physiology, Function, and Structure from Medical Images (MI'88)*, SPIE San Diego, CA, USA 2008.

[27] Heinzer, S., Worz, S., Kalla, C., Rohr, K., Weiss, M., A model for the self-organization of exit sites in the endoplasmic reticulum. *J. Cell Sci.* 2008, *121*, 55–64.

[28] Yeager, T. R., Neumann, A. A., Englezou, A., Huschtscha, L. I. et al., Telomerase-negative immortalized human cells contain a novel type of promyelocytic leukemia (PML) body. *Cancer Res.* 1999, *59*, 4175–4179.

[29] Cerone, M. A., Londono-Vallejo, J. A., Bacchetti, S., Telomere maintenance by telomerase and by recombination can coexist in human cells. *Hum. Mol. Genet.* 2001, *10*, 1945–1952.

[30] Fasching, C. L., Neumann, A. A., Muntoni, A., Yeager, T. R., Reddel, R. R., DNA Damage induces alternative lengthening of telomeres (ALT) associated promyelocytic leukemia bodies that preferentially associate with linear telomeric DNA. *Cancer Res.* 2007, *67*, 7072–7077.

[31] Dellaire, G., Eskiw, C. H., Dehghani, H., Ching, R. W. et al., Mitotic accumulations of PML protein contribute to the re-establishment of PML nuclear bodies in G1. *J. Cell Sci.* 2006, *119*, 1034–1042.

[32] Brouwer, A. K., Schimmel, J., Wiegant, J. C., Vertegaal, A. C. et al., Telomeric DNA mediates de novo PML body formation. *Mol. Biol. Cell* 2009, *20*, 4804–4815.

[33] Draskovic, I., Arnoult, N., Steiner, V., Bacchetti, S. et al., Probing PML body function in ALT cells reveals spatiotemporal requirements for telomere recombination. *Proc. Natl. Acad. Sci. USA* 2009, *106*, 15726–15731.

[34] Grobelny, J. V., Godwin, A. K., Broccoli, D., ALT-associated PML bodies are present in viable cells and are enriched in cells in the G(2)/M phase of the cell cycle. *J. Cell Sci.* 2000, *113*, 4577–4585.

[35] Wu, G., Lee, W. H., Chen, P. L., NBS1 and TRF1 colocalize at promyelocytic leukemia bodies during late S/G2 phases in immortalized telomerase-negative cells. *J. Biol. Chem.* 2000, *275*, 30618–30622.

[36] Jiang, W. Q., Zhong, Z. H., Nguyen, A., Henson, J. D. et al., Induction of alternative lengthening of telomeres-associated PML bodies by p53/p21 requires HP1 proteins. *J. Cell Biol.* 2009, *185*, 797–810.

[37] Shen, T. H., Lin, H.-K., Scaglioni, P. P., Yung, T. M., Pandolfi, P. P., The mechanisms of PML-nuclear body formation. *Mol. Cell* 2006, *24*, 331–339.

[38] Nacerddine, K., Lehembre, F., Bhaumik, M., Artus, J. et al., The SUMO pathway is essential for nuclear integrity and chromosome segregation in mice. *Dev. Cell* 2005, *9*, 769–779.

[39] Zeng, S., Xiang, T., Pandita, T. K., Gonzalez-Suarez, I. et al., Telomere recombination requires the MUS81 endonuclease. *Nat. Cell Biol.* 2009, *11*, 616–623.

[40] Stagno D'Alcontres, M., Mendez-Bermudez, A., Foxon, J. L., Royle, N. J., Salomoni, P., Lack of TRF2 in ALT cells causes PML-dependent p53 activation and loss of telomeric DNA. *J. Cell Biol.* 2007, *179*, 855–867.

Supporting information

A three-dimensional colocalization RNA interference screening platform to elucidate the alternative lengthening of telomeres pathway

Sarah Osterwald, Stefan Wörz, Jürgen Reymann, Frank Sieckmann, Karl Rohr, Holger Erfle and Karsten Rippe

Supporting materials and methods

Western blotting

Proteins were detected on nitrocellulose membranes with the following antibodies: mouse primary antibodies: anti-Ubc9 (1:1000, clone 50/Ubc9, BD Bioscience), anti-53BP1 (1:500, clone 19/53BP1, BD Bioscience), anti-ATM (1:500, #82314, Thermo Scientific), anti-TRF1 (1:500, clone TRF-78, GeneTex). Rabbit primary antibodies: anti-SUMO1 (1:500, #sc-9060, Santa Cruz Biotechnology), anti-Sp100 (1:500, #ab43151, Abcam), anti-SUMO2/3 (1:1000, #ab3742, Abcam).

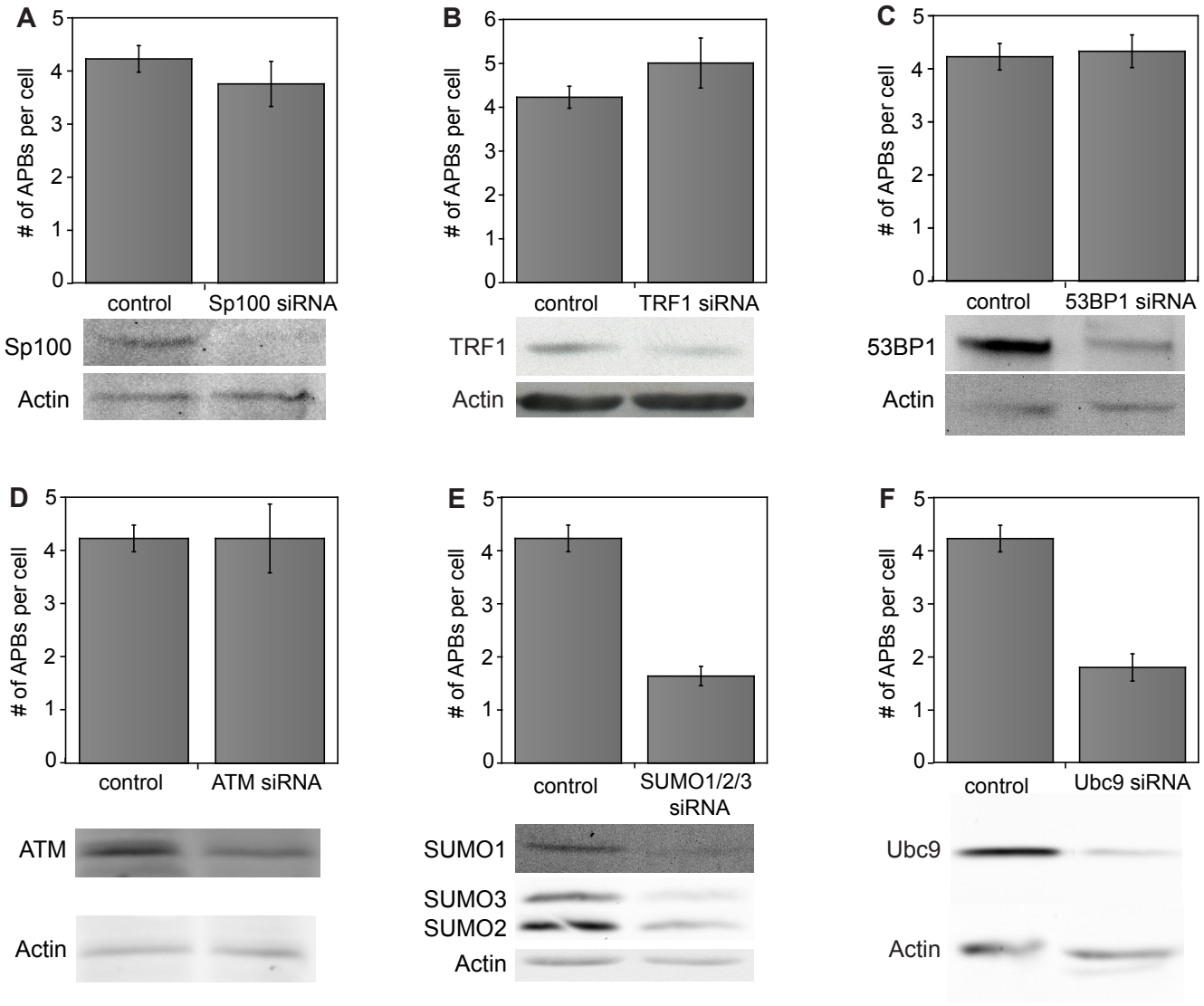

Figure S1. Manual assessment of controls as quality reference for the setup of the RNAi screen

The knockdown efficiency of the siRNA transfections was analyzed by western blotting. (A) Knockdown of Sp100 had no significant effect on the average number of APBs per cell. (B) Transfection with a siRNA targeting TRF1 resulted in a slight but not significant increase of the average number of APBs per cell. (C, D) RNAi-mediated knockdown of 53BP1 and ATM showed no significant change in the number of APBs per cell. (E) Upon knockdown of the three SUMO isoforms 1, 2 and 3 the average number of APBs per cell was reduced. (F) Transfection with Ubc9 siRNA led to a significant decrease in the number of APBs per cell. Error bars show the SEM.

siRNA	Experiment	# of cells	# of APBs per cell	Stdev. (# of APBs per cell)	$D_{n,n'}$ (KS test)	L_x (KS Test)	p-value KS test	p-value wilcox.test	p-value rateratio.test	p-value t.test
PML	48h_1	256	0.96	2.03	0.526	5.55	< 0.001	4.0E-33	4.7E-68	3.0E-22
	48h_2	178	0.85	1.77	0.647	5.99	< 0.001	1.1E-34	5.4E-85	1.1E-27
	48h_all	434	0.92	1.99	0.589	8.27	< 0.001	3.5E-65	2.3E-139	3.0E-45
	72h_1_1	310	1.04	1.64	0.615	7.88	< 0.001	2.9E-59	1.7E-163	1.7E-56
	72h_1_2	213	1.59	2.26	0.487	4.88	< 0.001	1.5E-25	1.7E-68	8.0E-18
	72h_2_1	196	0.80	1.72	0.550	5.43	< 0.001	3.1E-31	9.6E-73	9.3E-24
	72h_2_2	273	1.32	1.95	0.503	5.65	< 0.001	1.0E-33	1.5E-77	5.8E-28
	72h_all	992	1.17	1.90	0.524	11.61	< 0.001	5.7E-143	0	2.0E-115
MMS21	48h_1	135	3.64	3.01	0.070	0.62	> 0.1	0.42	0.096	0.27
	48h_2	148	3.57	3.36	0.147	1.30	0.05-0.1	0.056	0.064	0.24
	48h_all	301	3.27	3.13	0.140	1.79	0.0025-0.005	0.047	0.19	0.33
	72h_1_1	291	4.89	3.74	0.065	0.81	> 0.1	0.31	0.012	0.12
	72h_1_2	198	4.04	3.35	0.112	1.10	> 0.1	0.10	0.011	0.15
	72h_2_1	232	2.36	2.19	0.151	1.55	0.01-0.025	0.00015	3.1E-09	8.4E-05
	72h_2_2	216	3.94	3.26	0.064	0.68	> 0.1	0.58	0.95	0.95
	72h_all	937	3.80	3.20	0.067	1.46	0.025-0.05	0.0078	0.0029	0.064
Rad17	48h_1	169	3.43	3.12	-0.085	0.81	> 0.1	0.82	0.46	0.63
	48h_2	124	3.66	2.88	0.110	0.92	> 0.1	0.27	0.17	0.34
	48h_all	293	3.49	3.08	0.079	1.01	> 0.1	0.43	0.92	0.97
	72h_1_1	218	4.14	3.30	0.080	0.93	> 0.1	0.12	0.076	0.25
	72h_1_2	220	4.4	3.45	0.065	0.66	> 0.1	0.54	0.40	0.62
	72h_2_1	263	2.83	2.35	0.061	0.64	> 0.1	0.10	0.0026	0.040
	72h_2_2	260	4.61	2.87	-0.115	1.28	0.05-0.1	0.0032	0.00028	0.0086
	72h_all	961	3.99	3.02	-0.035	0.78	> 0.1	0.59	0.27	0.56
scrambled	48h_1	196	3.29	2.58						
	48h_2	166	3.99	2.83						
	48h_all	362	3.50	2.65						
	72h_1_1	350	4.46	3.13						
	72h_1_2	189	4.58	3.95						
	72h_2_1	195	3.33	2.76						
	72h_2_2	235	3.93	2.86						
	72h_all	969	4.07	3.12						

Table S1. Comparison of replicates and different statistical tests for the analysis of the number of APBs per cell (all classes)

The table contains the analysis of replicates of the three siRNAs shown in Fig. 8 with different statistical tests. The Kolmogorov-Smirnov and the Wilcoxon test were used as non-parametric tests, the rate ratio test as a test based on Poisson distribution and the student's t-test as a parametric test. The Kolmogorov-Smirnov was used for further statistical analysis because it reflects best the change in histograms and means upon RNAi-mediated gene knockdown.

siRNA	Experiment	# of cells	# of APBs per cell	Stdev. (# of APBs per cell)	$D_{n,n'}$ (KS test)	L_z (KS Test)	p-value KS test	p-value wilcox.test	p-value rateratio.test	p-value t.test
53BP1	48h_all 72h_all	350 752	2.99 3.48	3.10 2.85	0.156 0.078	2.08 1.60	< 0.001 0.01-0.025	8.0E-05 1.9E-05	0.00022 4.1E-10	0.019 4.4E-05
ATM	48h_all 72h_all	376 906	3.01 3.66	2.92 2.85	0.120 0.051	1.63 1.10	0.005-0.01 > 0.1	0.0014 0.0030	0.00021 7.4E-06	0.019 0.0027
MMS21	48h_all 72h_all	301 937	3.27 3.80	3.13 3.20	0.140 0.067	1.79 1.46	0.0025-0.005 0.025-0.05	0.047 0.0078	0.19 0.0029	0.33 0.064
no siRNA	48h_all 72h_all	446 1157	3.69 4.18	2.79 2.94	0.067 -0.042	0.95 0.96	> 0.1 > 0.1	0.30 0.15	0.12 0.22	0.31 0.44
PML	48h_all 72h_all	434 992	0.92 1.17	1.99 1.90	0.589 0.524	8.27 11.61	< 0.001 < 0.001	3.5E-65 5.7E-143	2.3E-139 0	3.0E-45 2.0E-115
Rad17	48h_all 72h_all	293 961	3.49 3.99	3.08 3.02	0.079 -0.035	1.01 0.78	> 0.1 > 0.1	0.43 0.59	0.92 0.27	0.97 0.56
Scrambled	48h_all 72h_all	362 969	3.50 4.07	2.65 3.12	0 0	0 0	1 1	1 1	1 1	1 1
Sp100	48h_all 72h_all	421 990	3.39 3.76	2.96 3.03	0.076 0.055	1.07 1.21	> 0.1 > 0.1	0.23 0.012	0.51 0.00078	0.60 0.024
SUMO 1/2/3	48h_all 72h_all	306 961	2.57 2.80	2.40 2.47	0.155 0.206	2.00 4.53	< 0.001 < 0.001	1.7E-06 7.0E-25	9.6E-12 2.3E-49	2.7E-06 9.4E-23
TRF1	48h_all 72h_all	214 688	3.26 4.61	2.74 3.24	0.078 -0.076	0.90 1.53	> 0.1 0.01-0.025	0.28 0.00015	0.12 3.8E-07	0.31 0.00084
Ubc9	48h_all 72h_all	327 976	2.82 2.45	2.67 2.27	0.127 0.242	1.67 5.33	0.005-0.01 < 0.001	7.6E-05 2.4E-39	5.9E-07 2.2E-84	0.00088 1.5E-37

Table S2. Overview of the effect of gene knockdown on the number of APBs per cell (all classes) assessed by different statistical methods.

The average effect over all replicates at one time point was analyzed by different statistical tests as indicated in Table S2.